IET Power Electronics

Research Article

IET Journals
The Institution of Engineering and Technology

Robust three-vector-based low-complexity model predictive current control with supertwisting-algorithm-based second-order sliding-mode observer for permanent magnet synchronous motor

ISSN 1755-4535
Received on 29th July 2018
Revised 13th June 2019
Accepted on 19th June 2019
E-First on 13th August 2019
doi: 10.1049/iet-pel.2018.5750
www.ietdl.org

Yanping Xu[1] ✉, *Xianhua Ding*[1], *Jibing Wang*[1], *Chen Wang*[1]

[1]*Department of Electrical Engineering, Xi'an University of Technology, Xi'an, People's Republic of China*

✉ *E-mail: xuyp@xaut.edu.cn*

Abstract: This study presents a robust three-vector-based low-complexity model predictive current control with supertwisting-algorithm-based second-order sliding-mode observer for permanent magnet synchronous motor (PMSM). First, to reduce the computational complexity of the three-vector-based model predictive current control, the optimal voltage vector combination is directly determined by the sector of desired voltage vector. Second, a supertwisting-algorithm-based second-order sliding-mode observer is designed to observe the lump disturbance caused by model mismatch and unmodelled dynamics. The estimated lump disturbance is considered as the compensation to the original PMSM model to reduce steady-state current error, which improves the robustness of the three-vector-based model predictive current control. Finally, the effectiveness of the proposed method is verified by experiments on a two-level-inverter-fed PMSM drive platform. Experimental results prove that, compared with three-vector-based model predictive current control, the proposed method can reduce the computational complexity and enhance robustness against motor parameters variation.

1 Introduction

The permanent magnet synchronous motor (PMSM) has been widely employed due to the advantages of small volume, simple structure and high efficiency [1–3]. With the wide application of the PMSM, its control method has also been attracted extensive attentions. Field oriented control (FOC) is one of the most common control methods for PMSM [4, 5]. FOC can achieve good steady-state performance. However, the parameters of multiple proportional integral (PI) regulators in FOC need to be adjusted and dynamic response of FOC needs to be further improved.

In recent years, model predictive control (MPC) has been widely applied in power electronics and power drives because of the fast dynamic response, simple principle and easy implementation, such as three-phase inverter [6, 7], pulse width modulation (PWM) rectifier [8, 9], matrix converter [10, 11], induction motor drive [12, 13] and PMSM drive [14]. In the traditional MPC, one voltage vector is applied during one sampling period. There are only seven selectable voltage vectors for a two-level voltage source inverter, so that the selection range of voltage vector is relatively small. This limits the steady-state performance of the traditional MPC [15]. In order to improve the steady-state performance of the traditional MPC, some scholars proposed a three-vector-based MPC [16, 17]. In this method, three voltage vectors are applied during one sampling period. However, this control method needs to find the optimal voltage vector combination and calculate the duration of each voltage vector in one sampling period. This process would generate heavy computational burden, which is one of the problems to be solved in the three-vector-based MPC.

Although the MPC has the fast dynamic response, it is sensitive to the motor parameters variation due to that the MPC is one of model-based control methods. In practical implementation, the influence of motor parameters variation and unmodelled dynamics is inevitable in the drive system. As a result, the model mismatch would happen, and this further causes the prediction error. Therefore, the voltage vector selected by the cost function maybe not the optimal voltage vector, which eventually leads to deteriorate system performance. In order to solve this problem, the prediction error correction is added to the predictive model to enhance robustness against stator inductance variation and consequently achieves better performance [18]. However, flux linkage of permanent magnets and stator resistance mismatch is not considered in this paper. In addition, the weight factors need to be adjusted when the predictive error correction is added to the predictive model, which increases the difficulty of system design and adjustment. The adaptive observer proposed in [19] and the extended Kalman filter proposed in [20] are used to identify motor parameters to overcome the adverse effects of parameter mismatch. However, online parameter identification leads to complicated computation. In [21], the disturbance observer is introduced into the MPC to observe the disturbance caused by the load variation and the motor parameters variation. The estimated disturbance is considered as compensation of motor model to improve the load disturbance rejection ability and robustness.

Among various disturbance observers, the sliding-mode observer is widely employed in disturbances observation owing to strong robustness [22–25]. However, the first-order sliding-mode observer has the disadvantage of obvious chattering phenomenon due to its own discontinuity, and this chattering phenomenon cannot be eliminated [26, 27]. The second-order sliding-mode observer, which is more suitable for system disturbances observation, can effectively reduce the chattering while maintaining good dynamic response [28–30]. In [31], the second-order sliding-mode observer is designed for permanent magnet linear synchronous machines to observe the lump disturbance, such as electromagnetic force ripple, detent force and unknown external disturbances. The estimated lump disturbance is considered as feedforward compensation, which can effectively suppress the force ripple.

A robust three-vector-based low-complexity model predictive current control with supertwisting-algorithm-based second-order sliding-mode observer (TV-LC-MPCC + STA-SMO) is proposed in this paper. Firstly, the optimal voltage vector combination is directly determined by the sector of desired voltage vector, which can reduce the computational complexity of the TV-MPCC. Secondly, a STA-SMO is designed to observe the lump

disturbance. The estimated lump disturbance is considered as compensation of original PMSM model. The original PMSM model is corrected to solve the problem of steady-state current error under parameter mismatch, which enhances the robustness against motor parameter mismatch. Finally, in order to verify the feasibility and effectiveness of the proposed method, the experimental tests were carried out on a two-level inverter fed PMSM drive system.

In this paper, the contributions of the proposed controller are: (i) the selection process of optimal voltage vector combination of the TV-MPCC is simplified, which reduces the computational complexity; (ii) the supertwisting-algorithm-based second-order sliding-mode observer is designed to observe the lump disturbance. The estimated lump disturbance is used to compensate the original PMSM model, so the problem of steady-state current error under parameter mismatch can be solved. Finally, the robustness against the motor parameters variation is effectively improved.

2 Model of PMSM

Assuming that the PMSM neglects stator core reluctance, rotor core reluctance, structural asymmetry, eddy current and hysteresis loss are not considered. The model of the surface-mounted PMSM in synchronous rotating frame is as follows:

$$\begin{aligned} &\frac{\mathrm{d}\boldsymbol{i}_\mathrm{s}}{\mathrm{d}t} = \boldsymbol{A}\boldsymbol{i}_\mathrm{s} + \boldsymbol{B}\boldsymbol{u}_\mathrm{s} + \boldsymbol{M} \\ &\boldsymbol{i}_\mathrm{s} = \begin{bmatrix} i_d & i_q \end{bmatrix}^\mathrm{T} \boldsymbol{u}_s = \begin{bmatrix} u_d & u_q \end{bmatrix}^\mathrm{T} \\ &\boldsymbol{A} = \begin{bmatrix} -\dfrac{R_\mathrm{s}}{L_\mathrm{s}} & \omega_{re} \\ -\omega_\mathrm{re} & -\dfrac{R_s}{L_s} \end{bmatrix}, \boldsymbol{B} = \begin{bmatrix} \dfrac{1}{L_\mathrm{s}} & 0 \\ 0 & \dfrac{1}{L_\mathrm{s}} \end{bmatrix}, \boldsymbol{M} = \begin{bmatrix} 0 \\ -\dfrac{\psi_\mathrm{f}}{L_\mathrm{s}}\omega_\mathrm{re} \end{bmatrix} \end{aligned} \tag{1}$$

where u_d and u_q are the d- and q-axis stator voltages, respectively. i_d and i_q are the d- and q-axis stator currents, respectively. ψ_f, L_s, R_s and ω_re denote the flux linkage of permanent magnets, stator inductance, stator resistance and rotor electrical angular velocity, respectively.

According to (1), the discrete model of PMSM can be obtained as

$$\boldsymbol{i}_\mathrm{s}(k+1) = (\boldsymbol{I} + \boldsymbol{A}T_\mathrm{s})\boldsymbol{i}_\mathrm{s}(k) + \boldsymbol{B}T_\mathrm{s}\boldsymbol{u}_\mathrm{s}(k) + T_\mathrm{s}\boldsymbol{M} \tag{2}$$

where $\boldsymbol{i}_\mathrm{s}(k+1)$ is the predicted stator current at $(k+1)$th sampling instant. $\boldsymbol{i}_\mathrm{s}(k)$, $\boldsymbol{u}_\mathrm{s}(k)$ and $\omega_\mathrm{re}(k)$ are the stator current, stator voltage and rotor electrical angular velocity at (k)th sampling instant, respectively.

3 TV-LC-MPCC method

3.1 TV-MPCC method

In the PMSM drive system fed by two-level voltage source inverter, there are six active voltage vectors ($\boldsymbol{u}_1$, $\boldsymbol{u}_2$, $\boldsymbol{u}_3$, $\boldsymbol{u}_4$, $\boldsymbol{u}_5$, $\boldsymbol{u}_6$) and two null vectors $\boldsymbol{u}_\mathrm{zero}$ ($\boldsymbol{u}_0$, $\boldsymbol{u}_7$). All active voltage vectors divide the space vector plane into six sectors as shown in Fig. 1. The TV-MPCC is proposed in [17], which applies three voltage vectors during one sampling period. In the TV-MPCC, two adjacent active voltage vectors and one null voltage vector are selected as a voltage vector combination within each sector; thus there are six voltage vector combinations in total. Moreover, the deadbeat principle of d-and q-axis currents is used to calculate the duration of each voltage vector. According to six voltage vector combinations and the duration of each voltage vector, six virtual voltage vectors can be synthesised. Then, six virtual voltage vectors are substituted into (2) to calculate the corresponding predicted current. Finally, all virtual voltage vectors can be evaluated through the cost function shown in (3). The virtual voltage vector minimising the cost function is selected as the optimal voltage vector. It can be seen that the TV-MPCC can obtain the optimal voltage vector combination by calculating the cost function for six times, which results in the heavy calculation burden.

$$g_i = \left|i_d^* - i_d(k+1)\right| + \left|i_q^* - i_q(k+1)\right| \tag{3}$$

where i_d* and i_q* are the d- and q-axis component of stator current reference, respectively.

In a real-time implementation, the sampling and the control algorithm take a significant portion of the sample period. This results in digital delay. The digital delay has adverse impact on the controller performance. Therefore $i_d(k+1)$ and $i_q(k+1)$ should be replaced by the values of the $i_d(k+2)$ and $i_q(k+2)$, which can compensate the digital delay in practical implementation [19]. Thus, the cost function should be rewritten as

$$g_i = \left|i_d^* - i_d(k+2)\right| + \left|i_q^* - i_q(k+2)\right| \tag{4}$$

3.2 TV-LC-MPCC method

In order to reduce the computational complexity of the TV-MPCC, the TV-LC-MPCC is proposed in this paper. The first step of the TV-LC-MPCC is to calculate the desired voltage vector $\boldsymbol{u}_\mathrm{s}$* based on the ideal of deadbeat control. Two adjacent active voltage vectors and one null vector in the sector of $\boldsymbol{u}_\mathrm{s}$* are selected as the optimal voltage vector combination, seeing Table 1 for details. Then the duration of each voltage vector is calculated by the deadbeat principle of d-and q-axis currents. The optimal voltage vector combination and duration are applied to the inverter. The TV-LC-MPCC can directly determine optimal voltage vector combination based on the sector of $\boldsymbol{u}_\mathrm{s}$*, thus reducing the computational burden.

In the TV-LC-MPCC, the first and most important step is to calculate the desired voltage vector. Let the predict stator current be equal to its reference as follows

$$\boldsymbol{i}_\mathrm{s}(k+1) = \boldsymbol{i}_\mathrm{s}^* \tag{5}$$

where $\boldsymbol{i}_\mathrm{s}$* is the stator current reference. Substituting (5) into (2), the desired voltage vector $\boldsymbol{u}_\mathrm{s}$* can be calculated as follows:

$$\boldsymbol{u}_\mathrm{s}^* = \frac{(\boldsymbol{i}_\mathrm{s}^* - \boldsymbol{i}_\mathrm{s}(k))}{\boldsymbol{B}T_\mathrm{s}} - \frac{\boldsymbol{A}\boldsymbol{i}_\mathrm{s}(k)}{\boldsymbol{B}} - \frac{\boldsymbol{M}(k)}{\boldsymbol{B}} \tag{6}$$

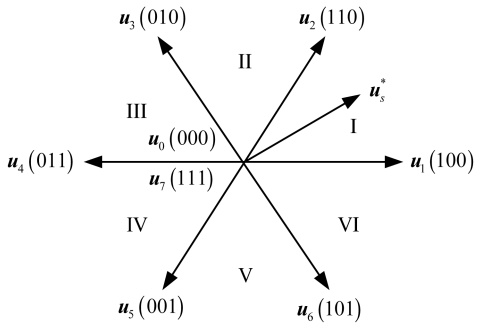

Fig. 1 *Basic voltage vectors of two-level inverter*

Table 1 Determining optimal voltage vector combination

Sector of $\boldsymbol{u}_\mathrm{s}$*	Optimal voltage vector combination
I	$\boldsymbol{u}_1$, $\boldsymbol{u}_2$ and $\boldsymbol{u}_\mathrm{zero}$ ($\boldsymbol{u}_0$ or $\boldsymbol{u}_7$)
II	$\boldsymbol{u}_2$, $\boldsymbol{u}_3$ and $\boldsymbol{u}_\mathrm{zero}$ ($\boldsymbol{u}_0$ or $\boldsymbol{u}_7$)
III	$\boldsymbol{u}_3$, $\boldsymbol{u}_4$ and $\boldsymbol{u}_\mathrm{zero}$ ($\boldsymbol{u}_0$ or $\boldsymbol{u}_7$)
IV	$\boldsymbol{u}_4$, $\boldsymbol{u}_5$ and $\boldsymbol{u}_\mathrm{zero}$ ($\boldsymbol{u}_0$ or $\boldsymbol{u}_7$)
V	$\boldsymbol{u}_5$, $\boldsymbol{u}_6$ and $\boldsymbol{u}_\mathrm{zero}$ ($\boldsymbol{u}_0$ or $\boldsymbol{u}_7$)
VI	$\boldsymbol{u}_6$, $\boldsymbol{u}_1$ and $\boldsymbol{u}_\mathrm{zero}$ ($\boldsymbol{u}_0$ or $\boldsymbol{u}_7$)

According to the sector of $\boldsymbol{u}_s$*, the optimal voltage vector combination ($\boldsymbol{u}_{opt1}$, $\boldsymbol{u}_{opt2}$, $\boldsymbol{u}_{zero}$) can be determined. The optimal voltage vector combination ($\boldsymbol{u}_{opt1}$, $\boldsymbol{u}_{opt2}$, $\boldsymbol{u}_{zero}$) consists of the two adjacent active voltage vectors and one null vector. After obtaining the optimal voltage vector combination ($\boldsymbol{u}_{opt1}$, $\boldsymbol{u}_{opt2}$, $\boldsymbol{u}_{zero}$), the duration of each voltage vector is calculated by the deadbeat principle of d-and q-axis currents

$$\begin{aligned}\boldsymbol{i}_s(k+1) &= \boldsymbol{i}_s(k) + s_{opt1}t_1 + s_{opt2}t_2 + s_0t_0 = \boldsymbol{i}_s^* \\ s_{opt1} &= \left[s_{opt1\_d}s_{opt1\_q}\right]^T,\ s_{opt2} = \left[s_{opt2\_d}s_{opt2\_q}\right]^T, s_0 = \left[s_{0\_d}s_{0\_q}\right]^T\end{aligned} \tag{7}$$

where s_{opt1_d}, s_{opt1_q}, s_{opt2_d}, s_{opt2_q}, s_{0_d} and s_{0_q} are, respectively, the slopes of the d- and q-axis currents when the voltage vectors $\boldsymbol{u}_{opt1}$, $\boldsymbol{u}_{opt2}$ and $\boldsymbol{u}_{zero}$ are applied. t_1, t_2 and t_0 are the duration of $\boldsymbol{u}_{opt1}$, $\boldsymbol{u}_{opt2}$ and $\boldsymbol{u}_{zero}$ during one sampling period.

The slopes of currents $\boldsymbol{s}_{opt1}$, $\boldsymbol{s}_{opt2}$ and $\boldsymbol{s}_0$ shown in (7) can be calculated according to (1) as follows:

$$\boldsymbol{s}_0 = \left.\frac{\mathrm{d}\boldsymbol{i}_s}{\mathrm{d}t}\right|_{\boldsymbol{u}_s=\boldsymbol{0}} = \boldsymbol{A}\boldsymbol{i}_s + \boldsymbol{M} \tag{8}$$

$$\boldsymbol{s}_{opt1} = \left.\frac{\mathrm{d}\boldsymbol{i}_s}{\mathrm{d}t}\right|_{\boldsymbol{u}_s=\boldsymbol{u}_{opt1}} = \boldsymbol{A}\boldsymbol{i}_s + \boldsymbol{B}\boldsymbol{u}_{opt1} + \boldsymbol{M} \tag{9}$$

$$\boldsymbol{s}_{opt2} = \left.\frac{\mathrm{d}\boldsymbol{i}_s}{\mathrm{d}t}\right|_{\boldsymbol{u}_s=\boldsymbol{u}_{opt2}} = \boldsymbol{A}\boldsymbol{i}_s + \boldsymbol{B}\boldsymbol{u}_{opt2} + \boldsymbol{M} \tag{10}$$

Substituting (8), (9) and (10) into (7), the duration of optimal voltage vector combination can be calculated as follows

$$\begin{aligned}t_1 = &\frac{e_d\left(s_{opt2\_q} - s_{0\_q}\right) + e_q\left(s_{0\_d} - s_{opt2\_d}\right)}{S} \\ &+ \frac{T_s\left(s_{0\_q}s_{opt2\_d} - s_{opt2\_q}s_{0\_d}\right)}{S}\end{aligned} \tag{11}$$

$$\begin{aligned}t_2 = &\frac{e_d\left(s_{0\_q} - s_{opt1\_q}\right) + e_q\left(s_{opt1\_d} - s_{0\_d}\right)}{S} \\ &+ \frac{T_s\left(s_{opt1\_q}s_{0\_d} - s_{0\_q}s_{opt1\_d}\right)}{S}\end{aligned} \tag{12}$$

$$t_0 = T_s - t_1 - t_2 \tag{13}$$

$$\begin{aligned}S = &s_{0\_q}s_{opt2\_q} + s_{opt1\_q}s_{0\_d} + s_{opt2\_q}s_{opt1\_d} \\ &- s_{opt1\_q}s_{opt2\_d} - s_{opt2\_q}s_{0\_d} - s_{0\_q}s_{opt1\_d}\end{aligned} \tag{14}$$

$$e_d = i_d^* - i_d(k) \tag{15}$$

$$e_q = i_q^* - i_q(k) \tag{16}$$

The optimal voltage vector combination ($\boldsymbol{u}_{opt1}$, $\boldsymbol{u}_{opt2}$, $\boldsymbol{u}_{zero}$) and the corresponding duration (t_1, t_2, t_0) are output to the pulse generator, which will further control the inverter.

4 Robust TV-LC-MPCC with STA-SMO

4.1 Design of STA-SMO

The sliding-mode observer has the advantages of easy realization and strong robustness, but the high frequency vibration near the sliding-mode surface causes sliding-mode chattering. The supertwisting algorithm (STA) is a second-order sliding-mode scheme that can suppress the chattering of the first-order sliding-mode observer. Therefore, the research on the STA-SMO has attracted extensive attention. In this paper, for purpose of observing lump disturbances caused by parameter mismatch and unmodelled dynamics, the STA-SMO is designed in the TV-LC-MPCC for PMSM drive system.

If the simplified system equation is described as follows:

$$\dot{x} = u + d \tag{17}$$

where x, u and d are the system-state variable, control input and disturbance, respectively. When the sliding surface is $s = x - \hat{x}$, according to the STA, the simplest form of STA-SMO is described as

$$\dot{\hat{x}} = u + \hat{d} - \lambda|s|^{\frac{1}{2}}\mathrm{sign}(s) \tag{18}$$

$$\dot{\hat{d}} = -\alpha\mathrm{sign}(s) \tag{19}$$

where $\hat{x}$ and $\hat{d}$ are the estimated values of x and d, respectively. In addition, $\alpha > 0$ and $\lambda > 0$ are the observer gains. sign is the sign function.

Taking unmodelled dynamics and parameter mismatch into consideration, the PMSM model given in (1) is rewritten as

$$\dot{\boldsymbol{i}}_s = \boldsymbol{A}\boldsymbol{i}_s + \boldsymbol{B}(\boldsymbol{u}_s - \boldsymbol{f}) + \boldsymbol{M} \tag{20}$$

where $f = [f_d f_q]^T$ is the lump disturbance, f_d and f_q are the $\boldsymbol{d}$- and q-axis disturbances caused by parameter mismatch and unmodelled dynamics, respectively. The lump disturbance f_d and f_q change slowly in steady-state. f_d and f_q can be written as

$$f_d = \triangle R_s i_d + \triangle L_s\frac{\mathrm{d}i_d}{\mathrm{d}t} - \triangle\triangle L_s\omega_{re}i_q + \varepsilon_d \tag{21}$$

$$f_q = \triangle R_s i_q + \triangle L_s\frac{\mathrm{d}i_q}{\mathrm{d}t} + \triangle L_s\omega_{re}i_d + \triangle\psi_f\omega_{re} + \varepsilon_q\,. \tag{22}$$

where ε_d and ε_q are the d- and q-axis unmodelled dynamics, respectively. In order to design a second-order sliding-mode disturbance observer based on STA, a variable is defined as

$$-\boldsymbol{B}\boldsymbol{f} = \boldsymbol{d} \tag{23}$$

Substituting (23) into (20), the PMSM model is rewritten as

$$\overset{g}{\boldsymbol{i}}_s = \boldsymbol{A}\boldsymbol{i}_s + \boldsymbol{B}\boldsymbol{u}_s + \boldsymbol{M} + \boldsymbol{d}\,. \tag{24}$$

Applying the STA-SMO (18) and (19) into (24), the STA-SMO is finally designed as

$$\dot{\hat{\boldsymbol{i}}}_s = \boldsymbol{A}\hat{\boldsymbol{i}}_s + \boldsymbol{B}\boldsymbol{u}_s + \boldsymbol{M} + \hat{d} - k_1|s|^{\frac{1}{2}}\mathrm{sign}(s) \tag{25}$$

$$\dot{\hat{\boldsymbol{d}}} = -k_2\mathrm{sign}(s) \tag{26}$$

where $s = [s_d\ s_q]^T$, $s_d = i_d - \hat{i}_d$, $s_q = i_q - \hat{i}_q$. k_1 and k_2 are the designed observer gains.

Discreting (25) and (26), thus the discrete STA-SMO can be expressed as

$$\begin{aligned}\hat{i}_s(k+1) = &(I + T_s\boldsymbol{A})\hat{i}_s(k) + T_s\boldsymbol{B}\boldsymbol{u}_s(k) + T_s\boldsymbol{M}(k) \\ &+ T_s\hat{d}(k) - k_1T_s|s(k)|^{\frac{1}{2}}\mathrm{sign}(s(k))\end{aligned} \tag{27}$$

$$\hat{d}(k+1) = \hat{d}(k) - k_2T_s\mathrm{sign}(s(k)) \tag{28}$$

According to (23), the estimated lump disturbance is

$$\hat{\boldsymbol{f}}(k) = -\frac{1}{\boldsymbol{B}}\hat{\boldsymbol{d}}(k) \tag{29}$$

Fig. 2 illustrates the block diagram of discrete STA-SMO.

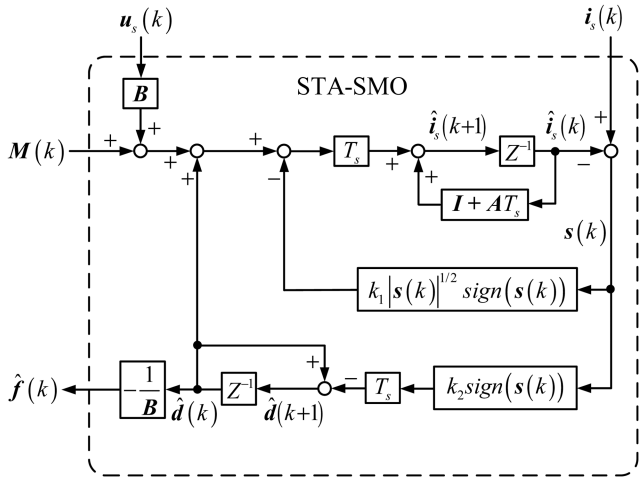

Fig. 2 *Block diagram of the STA-SMO*

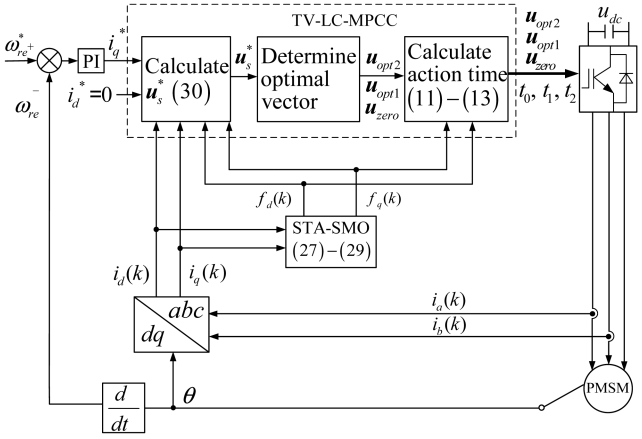

Fig. 3 *Block diagram of the TV-LC-MPCC + STA-SMO method for PMSM*

4.2 Robust TV-LC-MPCC with STA-SMO

After adding the lump disturbance estimated by the STA-SMO, (6), (8), (9) and (10) of the TV-LC-MPCC should be rewritten as

$$\boldsymbol{u}_s^* = \frac{(\boldsymbol{i}_s^* - \boldsymbol{i}_s(k))}{\boldsymbol{B}T_s} - \frac{\boldsymbol{A}\boldsymbol{i}_s(k)}{\boldsymbol{B}} - \frac{\boldsymbol{M}(k)}{\boldsymbol{B}} + \hat{\boldsymbol{f}} \tag{30}$$

$$s_0 = \left.\frac{\mathrm{d}\boldsymbol{i}_s}{\mathrm{d}t}\right|_{u_s=\boldsymbol{0}} = \boldsymbol{A}\boldsymbol{i}_s - \boldsymbol{B}\hat{\boldsymbol{f}} + \boldsymbol{M} \tag{31}$$

$$s_{\mathrm{opt1}} = \left.\frac{\mathrm{d}\boldsymbol{i}_s}{\mathrm{d}t}\right|_{\boldsymbol{u}_s=\boldsymbol{u}_{\mathrm{opt1}}} = \boldsymbol{A}\boldsymbol{i}_s + \boldsymbol{B}\left(\boldsymbol{u}_{\mathrm{opt1}} - \hat{\boldsymbol{f}}\right) + \boldsymbol{M} \tag{32}$$

$$s_{\mathrm{opt2}} = \left.\frac{\mathrm{d}\boldsymbol{i}_s}{\mathrm{d}t}\right|_{\boldsymbol{u}_s=\boldsymbol{u}_{\mathrm{opt2}}} = \boldsymbol{A}\boldsymbol{i}_s + B\left(u_{\mathrm{opt2}} - \hat{\boldsymbol{f}}\right) + \boldsymbol{M} \tag{33}$$

After adding the estimated lump disturbance, the optimal voltage vector combination can be re-determined by the desired voltage vector $\boldsymbol{u}_s$* in (30). Then (31), (32) and (33) are the current slopes when estimated disturbance is added to the PMSM model. These current slopes are combined with (7), and the duration t_1, t_2 and t_0 can be calculated through (11)–(13). Finally, the re-determined optimal voltage vector combination ($\boldsymbol{u}_{\mathrm{opt1}}$, $\boldsymbol{u}_{\mathrm{opt2}}$, $\boldsymbol{u}_{\mathrm{zero}}$) and the corresponding duration (t_1, t_2, t_0) are output to the pulse generator. Fig. 3 is the block diagram of the TV-LC-MPCC + STA-SMO control system.

4.3 Stability analysis of STA-SMO

The stability of the STA-SMO observer is analysed in [29, 32]. As analysed in [32], a function $\Phi(\alpha, \lambda, C) = |\Psi(t_*)|$ should be defined, where $(\sum(t), \Psi(t))$ is the solution of $\dot{\sum} = -|\sum|^{\frac{1}{2}} + \Psi$,

$$\dot{\Psi} = \begin{cases} -\frac{1}{k_1^2}(k_2 - C), & -\left|\sum\right|^{\frac{1}{2}} + \Psi > 0, \\ -\frac{1}{k_1^2}(k_2 + C), & -\left|\sum\right|^{\frac{1}{2}} + \Psi \le 0, \end{cases} \quad \sum(0) = 0,\ \Psi(0) = 1 \tag{34}$$

where $k_2 > C > 0$, C is Lipschitz's constant. $k_1 \neq 0$, and $t_* = \inf\{t/t > 0, \Sigma(t) = 0, \Psi(t) < 0\}$. According to the convergence criterion in [32], the observer can converge when the defined function $\Phi(k_1, k_2, C) < 1$ and $k_1 > 0$. In contrast, it does not converge if $\Phi(k_1, k_2, C) > 1$. The smaller $\Phi(k_1, k_2, C)$ makes the faster convergence. Finally, the sufficient conditions for the convergence of observer are

$$\begin{cases} k_2 > C \\ k_1^2 \ge \dfrac{4C(k_2 + C)}{(k_2 - C)} \end{cases} \tag{35}$$

It can be seen from (34) that increasing k_1 causes decrease of $\Phi(k_1, k_2, C)$, therefore increasing k_1 can make the faster convergence. Generally, the gain k_1 is more effective in the response time, while the gain k_2 has greater influence on steady-state control accuracy [33].

The equation mentioned above is only a sufficient condition for the stability of STA-SMO. In order to further analyse the necessary and sufficient conditions for the stability of STA-SMO, firstly, the

Lyapunov function is defined as $V = s^2(k)$ according to the analysis in literature [29, 34], yields

$$\begin{aligned} \triangle V &= s^2(k+1) - s^2(k) \\ &= [s(k+1) - s(k)][s(k+1) + s(k)] \end{aligned} \tag{36}$$

Multiplying (36) by $\text{sign}^2(s(k))$ can obtain the necessary and sufficient conditions for the existence of the sliding-mode hyperplane as follows:

$$\begin{cases} [s(k+1) - s(k)]\text{sign}(s(k)) < 0 \\ [s(k+1) + s(k)]\text{sign}(s(k)) \geq 0 \end{cases} \tag{37}$$

The stability of STA-SMO can be ensured through the select of the observer gain according to (35) and (37).

5 Experimental results

To validate the performance of the proposed method, the experiments are performed on the Expert3 system based on the TMS320C6713 digital signal processor (DSP). The Expert3 system is produced by Myway Company. The block diagram of experimental test bench is presented in Fig. 4. The main circuit consists of a three-phase six diode rectifier and a two-level voltage source inverter. The output of the inverter is connected to one PMSM which is used for testing the proposed method. The parameters of the PMSM are shown in Table 2.The other PMSM is controlled by the load supply system, which provides load torque. The DSP board mainly performs core algorithm calculation. The PEV board includes PWM generator, A/D converter, D/A converter and counter. The voltage is measured by a voltage sensor while the currents are measured by current sensors. The rotor mechanical position is obtained through an incremental encoder. An oscilloscope is used to monitor the control variables through the D/A converter. The experimental setup is shown in Fig. 5. The sampling frequency of current loop is 10 kHz in experiments. The

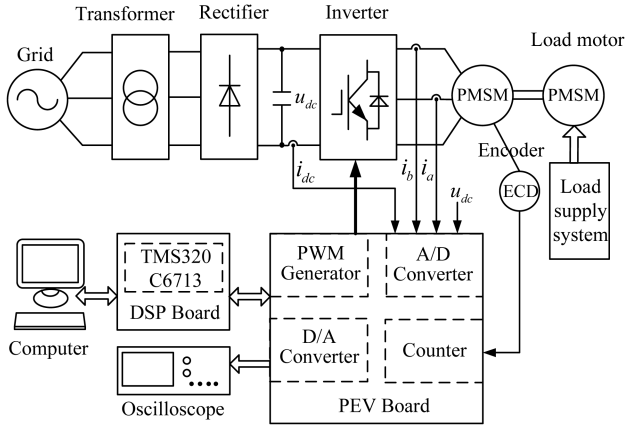

Fig. 4 *Block diagram of experimental test bench*

Table 2 Parameters of the PMSM

Description	Parameters	Values
flux linkage of permanent magnets	ψ_f	0.253 Wb
stator inductance	L_s	21.7 mH
stator resistance	R_s	2.725Ω
rated torque	T_N	9.6 Nm
rated speed	n	2430 r/min
number of pole pairs	P_n	4
rotational inertia	J	0.0011 kg m^2
rated current	I_N	4.4 A
rated power	P_N	2.4 kW
rated voltage	U_N	382 V

PI controller of speed loop is tuned as $k_p = 0.055$, $k_i = 0.0003$. The gain of the STA-SMO is chosen as $k_1 = 0.21$, $k_2 = 114$.

5.1 Verification of TV-LC-MPCC performance

In order to verify the advantage of TV-LC-MPCC method in reducing computational burden, the TV-LC-MPCC and TV-MPCC are compared by experiments.

First, the experimental responses to a step change in the load at 1000 r/min are shown in Fig. 6. The test scenario is: the load steps from no load to rated load at 2.0 s. It can be seen that both TV-LC-MPCC and TV-MPCC can quickly follow the load change. The d- and q-axis current ripple can be calculated by (38) and (39)

$$i_{d\_\text{ripple}} = \sqrt{\frac{1}{N}\sum_{n=1}^{N}\left(i_d(n) - i_{d\_\text{ave}}(n)\right)^2} \tag{38}$$

$$i_{q\_\text{ripple}} = \sqrt{\frac{1}{N}\sum_{n=1}^{N}\left(i_q(n) - i_{q\_\text{ave}}(n)\right)^2} \tag{39}$$

where N is the number of samples, $i_d(n)$ and $i_q(n)$ are d- and q-axis currents, respectively, which is obtained from the oscilloscope. i_{d_ave} and i_{q_ave} are the average values of d-and q-axis currents, respectively. The experimental data of 3.2–4 s in Fig. 6 are used to calculate d- and q-axis current ripple by (38) and (39). From the calculation, the results show that the d-axis current ripple of both TV-MPCC and TV-LC-MPCC method is 0.18 A, and the q-axis current ripple is 0.21 A. From the above experimental results and analysis, a conclusion can be drawn that the TV-LC-MPCC and TV-MPCC method have the same dynamic and static responses.

Second, the core algorithm program execution time of the TV-MPCC and TV-LC-MPCC methods is tested by experiments. The results are shown in Table 3. As can be seen from Table 3, the algorithm execution time of the TV-MPCC is 38.5 μs, while the algorithm execution time of TV-LC-MPCC is only 8.8 μs. The computational burden of the TV-LC-MPCC is reduced by 77% compared with TV-MPCC, because the TV-LC-MPCC can directly determine the optimal voltage vector combination according to the sector of $\boldsymbol{u}_s$*. However, the TV-MPCC needs to calculate the cost function for six times in each sampling period to obtain the optimal voltage vector combination.

From the analysis of the above experiment results, it can be drawn that, compared with TV-MPCC, the TV-LC-MPCC reduces computational burden while maintains the same good dynamic and static response.

5.2 Verification of TV-LC-MPCC + STA-SMO performance under parameter mismatch

To verify the robustness of the proposed TV-LC-MPCC + STA-SMO under parameter mismatch, the TV-LC-MPCC + STA-SMO and the TV-LC-MPCC are compared by experiments. The flux linkage of permanent magnetsψ_f, stator inductance L_s and stator resistance R_s are selected as test parameters. The motor parameters

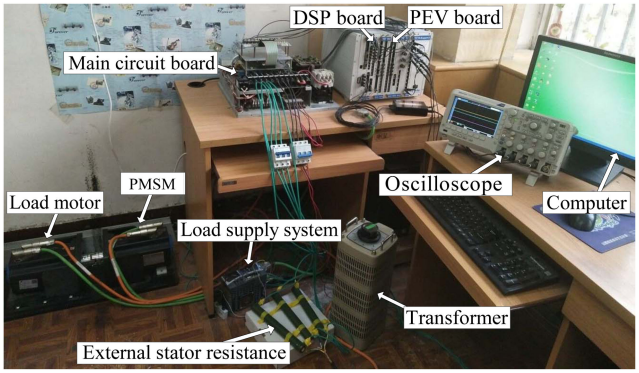

Fig. 5 *Experimental setup*

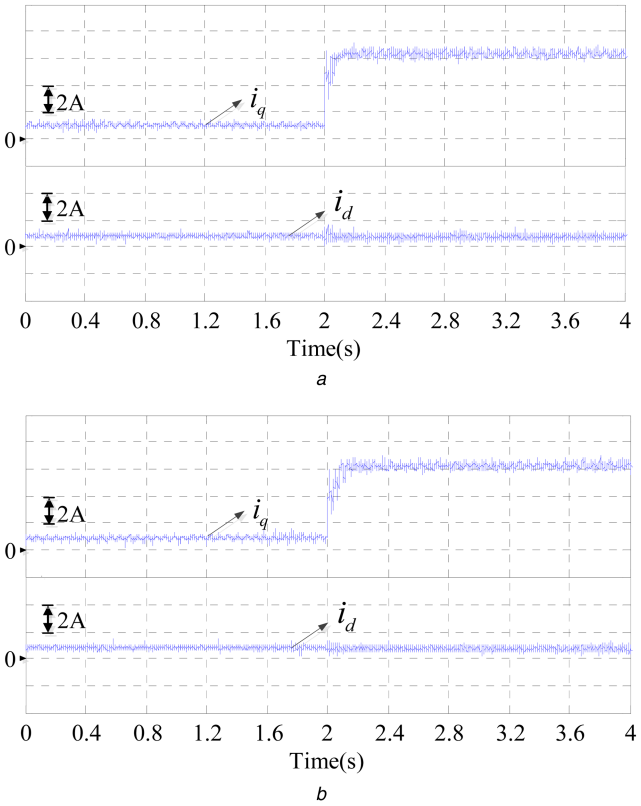

Fig. 6 *Experimental results of the TV-MPCC and TV-LC-MPCC under a step change in the load*
(a) TV-MPCC, ***(b)*** TV-LC-MPCC

Table 3 Computational burden of two methods

Methods	Optimisation times	Execution time, μs
TV-MPCC	6	38.5
TV-LC-MPCC	1	8.8

variation is divided into three steps. Since the rated parameters ψ_{f0}, L_{s0} and R_{s0} of the PMSM cannot be changed freely, the parameter mismatch test is completed by modifying the motor parameters in the controller. The waveforms of d- and q- axis currents i_d, i_q and their reference i_d*, i_q* are given in Figs. 7–9. Additionally, the estimated lump disturbance $\hat{f}_d$ and $\hat{f}_q$ are also provided in Fig. 7*b*, Figs. 8*b* and 9*b*. The d- and q-axis steady-state current error can be calculated by (40) and (41). The calculation results are shown in Table 4

$$\Delta i_d = \frac{1}{N}\sum_{n=1}^{N}\left|i_d(n) - i_d^*(n)\right| \tag{40}$$

$$\Delta i_q = \frac{1}{N}\sum_{n=1}^{N}\left|i_q(n) - i_q^*(n)\right| \tag{41}$$

It can be seen from Fig. 7*a* that, in the TV-LC-MPCC method, both d- and q-axis have steady-state current error under the flux linkage of permanent magnets mismatch. The influence of the flux linkage of permanent magnets mismatch on the q-axis steady-state current error is obvious. Especially when flux linkage of permanent magnets becomes $2\psi_{f0}$, the q-axis steady-state current error is 1.29 A. In contrast, i_d and i_q can follow their references in the TV-LC-MPCC + STA-SMO method, as shown in Fig. 7*b*. It can be drawn from Table 4 that the TV-LC-MPCC + STA-SMO can obviously reduce the d-and q-axis steady-state current error caused by flux linkage of permanent magnets mismatch. The estimated disturbance $\hat{f}_d$ and $\hat{f}_q$ are considered as compensation and can adjust the controller to suppress steady-state current error.

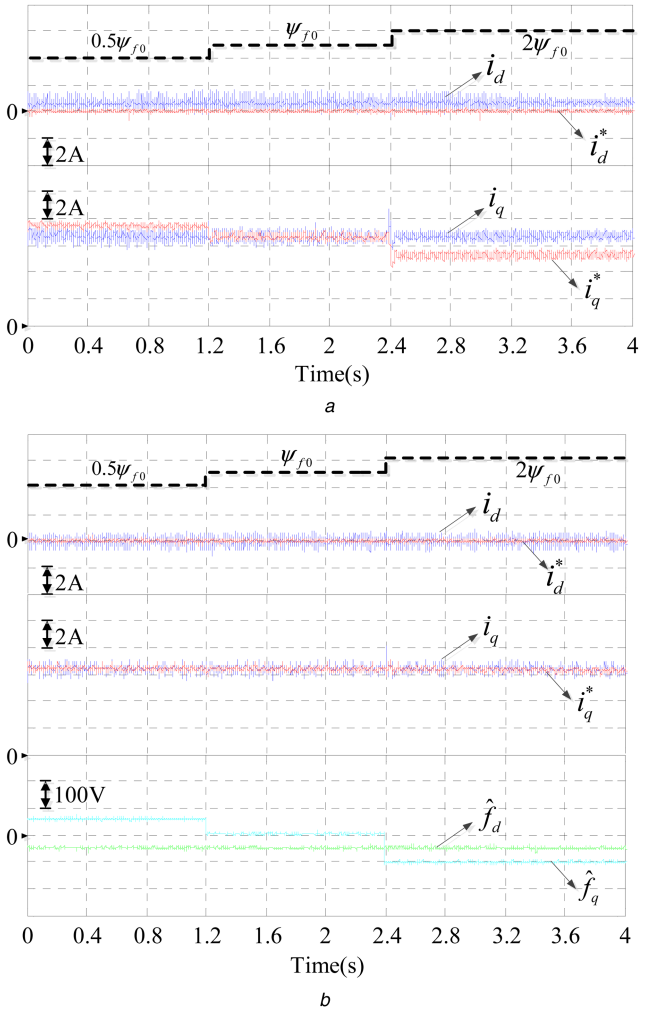

Fig. 7 *Experimental results of the TV-LC-MPCC and TV-LC-MPCC + STA-SMO at 1000 r/min with rated load under flux linkage of permanent magnets mismatch*
(a) TV-LC-MPCC, ***(b)*** TV-LC-MPCC + STA-SMO

Fig. 8*a* illustrates the performance of the TV-LC-MPCC under stator inductance mismatch. It reveals that i_d and i_q cannot track their references under stator inductance mismatch. The influence of the stator inductance mismatch on the d-axis steady-state current error is obvious. In particular, the d-axis steady-state current error is 1.13 A when the stator inductance becomes $0.7L_{s0}$. Fig. 8*b* presents the performance of the LC-MPCC + STA-SMO under stator inductance mismatch. i_d and i_q can track their references using the TV-LC-MPCC + STA-SMO method, as shown in Fig. 8*b*. The disturbance $\hat{f}_d$ and $\hat{f}_q$ estimated by STA-SMO are shown in Fig. 8*b*. It is proved that the STA-SMO can accurately observe the disturbance caused by the stator inductance mismatch.

It can be seen from Fig. 9*a* that, when using the TV-LC-MPCC method, stator resistance mismatch has less influence on the d- and q-axis steady-state current error compared with stator inductance mismatch and flux linkage of permanent magnets mismatch. Nevertheless, steady-state current error between the d- and q-axis currents and their references still exists. However, when the proposed TV-LC-MPCC + STA-SMO is applied in the PMSM, the STA-SMO can accurately observe the disturbance caused by the stator resistance mismatch as shown in Fig. 9*b*. Therefore, the d- and q-axis currents can follow their references as shown in Fig. 9*b*, and the robustness against stator resistance mismatch is improved.

To further verify the robustness of the proposed method, a test is completed by connecting external stator resistance with the motor terminal. The value of external stator resistance is 10 Ω. The PMSM is operated at 1000 r/min with 8 N m load. The three external stator resistances are connected with the motor terminal at 2.0 s. Experimental results are shown in Fig. 10. It can be seen

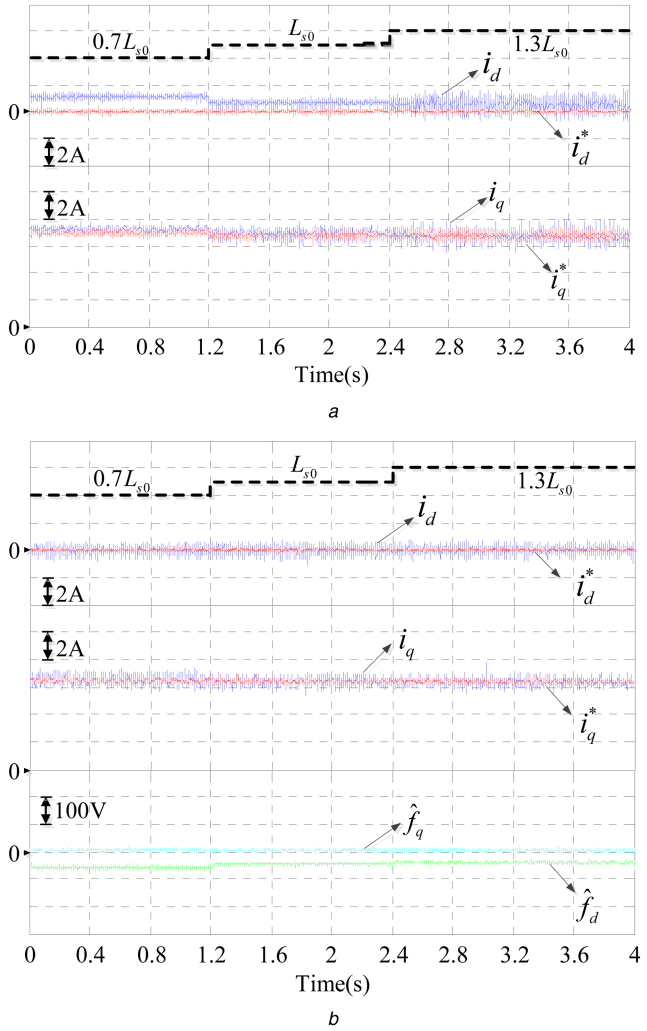

Fig. 8 *Experimental results of the TV-LC-MPCC and TV-LC-MPCC + STA-SMO at 1000 r/min with rated load under stator inductance mismatch*
(a) TV-LC-MPCC, ***(b)*** TV-LC-MPCC + STA-SMO

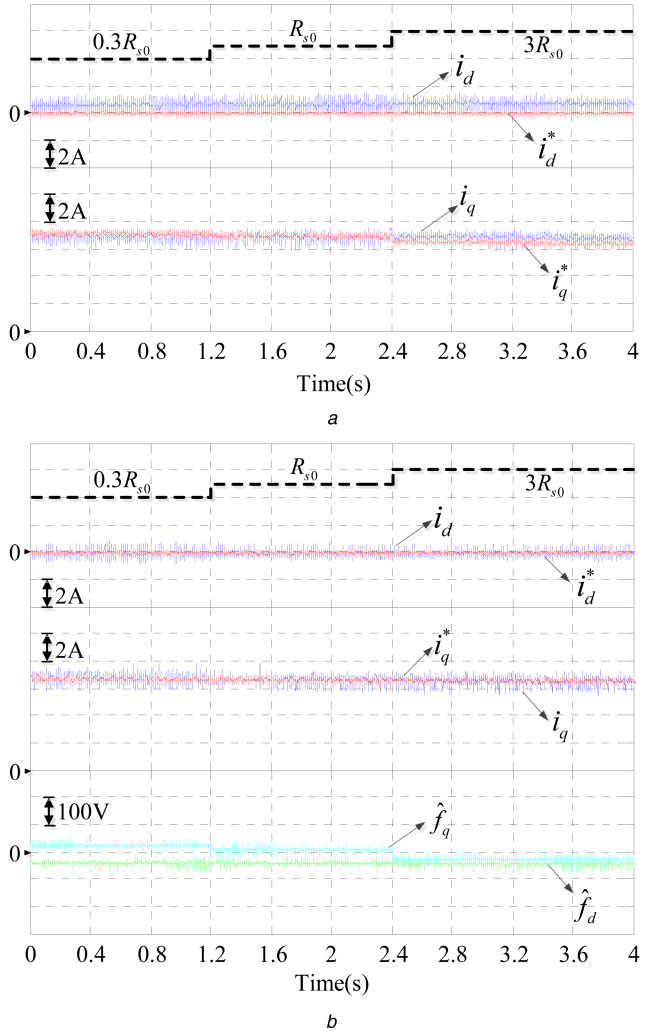

Fig. 9 *Experimental results of the TV-LC-MPCC and TV-LC-MPCC + STA-SMO at 1000 r/min with rated load under stator resistance mismatch*
(a) TV-LC-MPCC, ***(b)*** TV-LC-MPCC + STA-SMO

from Fig. 10*a* that i_d and i_q cannot track their references in the TV-LC-MPCC when three external stator resistances are connected with the motor terminal. In particular, the q-axis steady-state current error is 0.81 A when three external stator resistances are connected with the motor terminal. In addition, the speed slightly decreases and the torque changes slightly in the TV-LC-MPCC when three external stator resistances are connected with the motor terminal. However, i_d and i_q can track their references in the TV-LC-MPCC + STA-SMO when three external stator resistances are connected with the motor terminal, as shown in Fig. 10*b*. The speed and torque are still stable when three external stator resistances are connected with the motor terminal.

Fig. 7*a*, Figs. 8*a*, 9*a* and 10*a* illustrate that the TV-LC-MPCC has d- and q-axis steady-state current error under the motor parameter mismatch, while Fig. 7*b*, Figs. 8*b*, 9*b* and 10*b* demonstrate that i_d and i_q can track their references when the TV-LC-MPCC + STA-SMO is applied under motor parameter mismatch. The reason is that the STA-SMO is designed in the TV-LC-MPCC + STA-SMO to observe the lump disturbance. The estimated lump disturbance is considered as compensation of original PMSM model, which can obviously reduce steady-state current error under motor parameter mismatch, thus improving the robustness against the motor parameter mismatch.

5.3 Verification of TV-LC-MPCC + STA-SMO performance

Fig. 11 is the experimental results of the TV-LC-MPCC + STA-SMO at 20 r/min with no load. Fig. 12 is the experimental results of the TV-LC-MPCC + STA-SMO at zero speed with no load. The experimental results include the waveform of speed, d- and q-axis currents and phase current i_a. It can be seen from Figs. 11 and 12 that the PMSM operates stably by using the proposed method at 20 r/min and zero speed as well.

In order to test the performance of the TV-LC-MPCC + STA-SMO with variations on speed, the speed reference is set as four step changes: 500, 1000, 1500 and 2000 r/min. The experimental waveforms of the speed and the d- and q-axis currents are shown in Fig. 13. As demonstrated in Fig. 13, the speed of the PMSM can quickly track its reference.

Table 4 Steady-state current error of two control methods under parameter mismatch

Method	Parameter mismacth	Δi_d, A	Δi_q,A
TV-LC-MPCC	$\psi_f = 0.5\psi_{f0}$	0.70	0.83
TV-LC-MPCC + STA-SMO		0.01	0.01
TV-LC-MPCC	$\psi_f = 2\psi_{f0}$	0.76	1.29
TV-LC-MPCC + STA-SMO		0.01	0.01
TV-LC-MPCC	$L_s = 0.7L_{s0}$	1.13	0.10
TV-LC-MPCC + STA-SMO		0.02	0.01
TV-LC-MPCC	$L_s = 1.3L_{s0}$	0.51	0.04
TV-LC-MPCC + STA-SMO		0.02	0.02
TV-LC-MPCC	$R_s = 0.3R_{s0}$	0.65	0.22
TV-LC-MPCC + STA-SMO		0.02	0.02
TV-LC-MPCC	$R_s = 3R_{s0}$	0.81	0.44
TV-LC-MPCC + STA-SMO		0.02	0.02

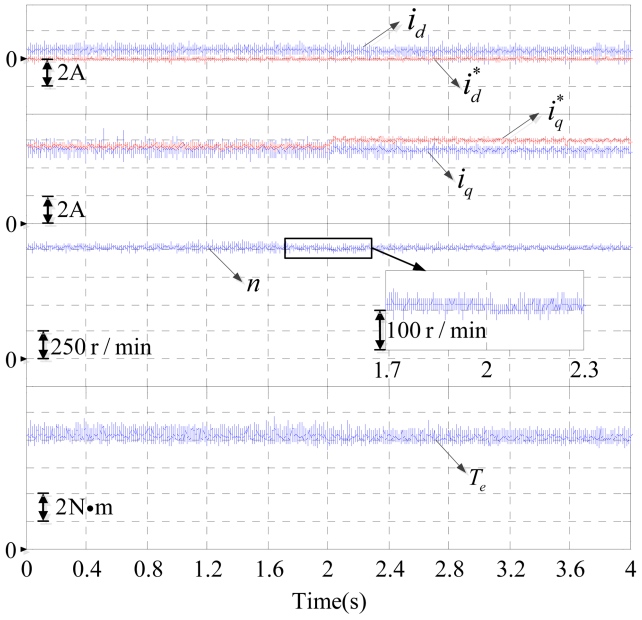

a

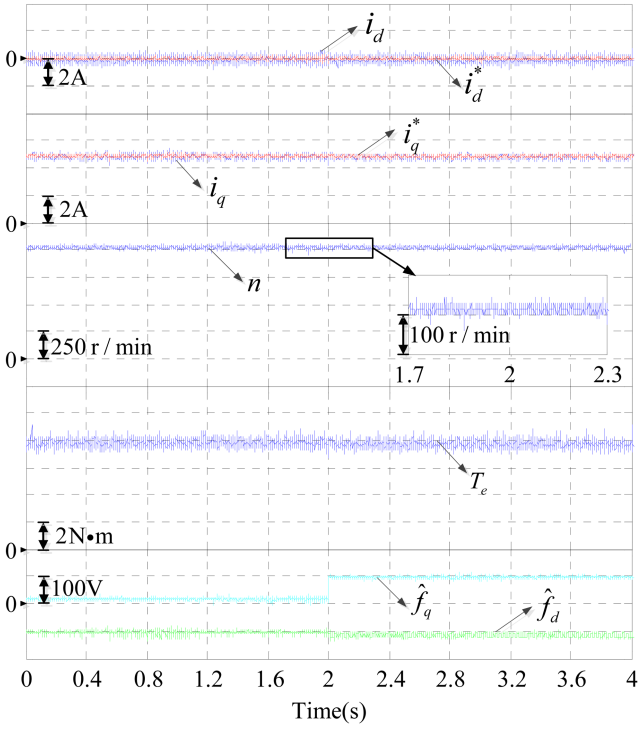

b

Fig. 10 *Experimental results of the TV-LC-MPCC and TV-LC-MPCC + STA-SMO under connecting external stator resistance with the motor terminal*

(a) TV-LC-MPCC, ***(b)*** TV-LC-MPCC + STA-SMO

6 Conclusions

In this paper, aiming at large computational burden and steady-state current error under parameter mismatch of the three-vector-based MPCC, a robust three-vector-based low-complexity MPCC with STA-SMO is proposed. In order to reduce the computational complexity, the optimisation process of optimal voltage vector combination in the three-vector-based MPCC is simplified. Moreover, the STA-SMO was designed to observe the lump disturbance caused by the parameter mismatch and unmodelled dynamics. The estimated lump disturbance is considered as compensation to the PMSM model, which suppresses steady-state current error caused by lump disturbance. The experimental results show that the three-vector-based low-complexity MPCC can reduce the computational burden while maintaining the same good

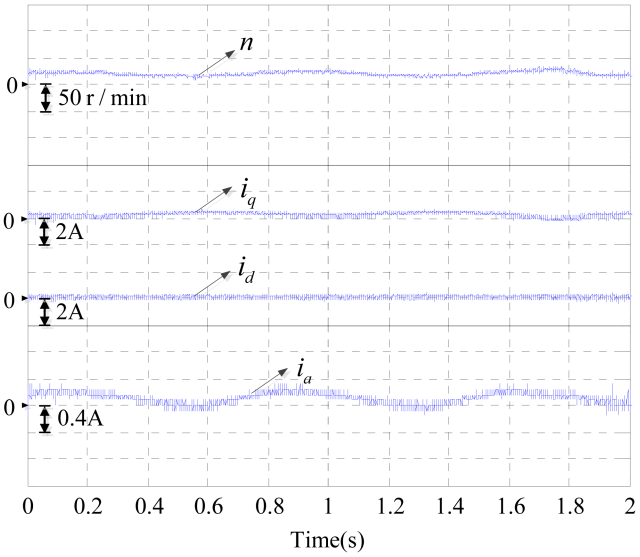

Fig. 11 *Experimental results of the TV-LC-MPCC + STA-SMO at 20 r/min with no load*

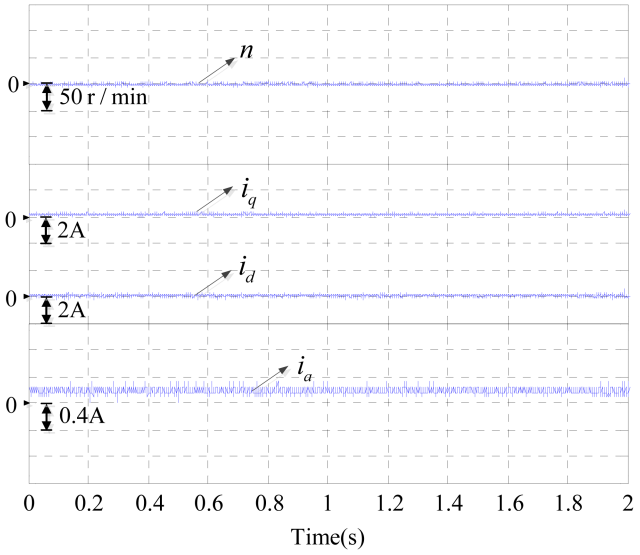

Fig. 12 *Experimental results of the TV-LC-MPCC + STA-SMO at zero speed with no load*

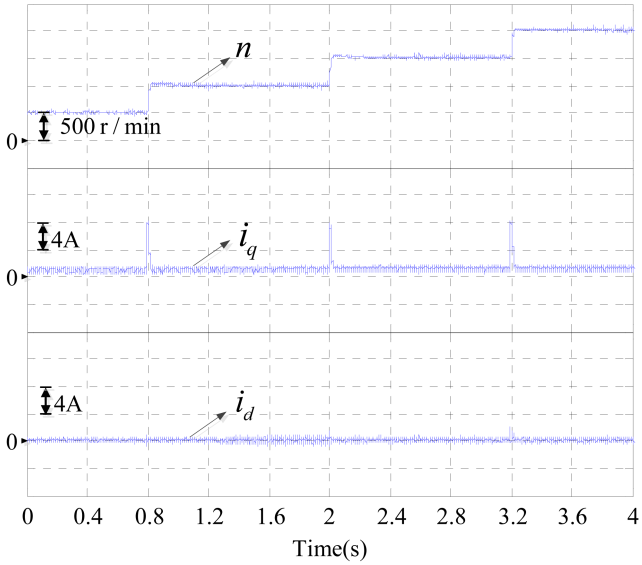

Fig. 13 *Experimental results of the TV-LC-MPCC + STA-SMO under step changes in the speed*

dynamic and static response compared with the three-vector-based MPCC. The *d*- and *q*-axis current of the proposed robust three-vector-based low-complexity MPCC with STA-SMO can follow their references under parameter mismatch; thus improving robustness against the flux linkage of permanent magnets, stator inductance and stator resistance mismatch.

7 References

[1] Zhang, J., Yang, H., Wang, T., *et al.*: 'Field-oriented control based on hysteresis band current controller for a permanent magnet synchronous motor driven by a direct matrix converter', *IET Power Electron.*, 2018, **11**, (7), pp. 1277–1285

[2] Mendoza-Mondragón, F., Hernández-Guzmán, V.M., Rodríguez-Reséndiz, J.: 'Robust speed control of permanent magnet synchronous motors using two-degrees-of-freedom control', *IEEE Trans. Ind. Electron.*, 2018, **65**, (8), pp. 6099–6108

[3] Zhang, J., Yang, H., Wang, T., *et al.*: 'Development of a prime mover emulator using a permanent-magnet synchronous motor drive', *IEEE Trans. Power Electron.*, 2018, **33**, (7), pp. 6114–6125

[4] Wang, Z., Chen, J., Cheng, M., *et al.*: 'Field-oriented control and direct torque control for paralleled VSIs fed PMSM drives with variable switching frequencies', *IEEE Trans. Power Electron.*, 2016, **31**, (3), pp. 2417–2428

[5] Lara, J., Xu, J.M., Chandra, A.: 'Effects of rotor position error in the performance of field-oriented-controlled PMSM drives for electric vehicle traction applications', *IEEE Trans. Ind. Electron.*, 2016, **63**, (8), pp. 4738–4751

[6] Nguyen, H.T., Kim, E.-K., Kim, I.-P., *et al.*: 'Model predictive control with modulated optimal vector for a three-phase inverter with an LC filter', *IEEE Trans. Power Electron.*, 2018, **33**, (3), pp. 2690–2703

[7] Nauman, M., Hasan, A.: 'Efficient implicit model-predictive control of a three-phase inverter with an output LC filter', *IEEE Trans. Power Electron.*, 2016, **31**, (9), pp. 6075–6078

[8] Song, W., Deng, Z., Wang, S., *et al.*: 'A simple model predictive power control strategy for single-phase PWM converters with modulation function optimization', *IEEE Trans. Power Electron.*, 2016, **31**, (7), pp. 5279–5289

[9] Tao, Y., Wu, Q., Wang, L., *et al.*: 'Voltage sensorless predictive direct power control of three-phase PWM converters', *IET Power Electron.*, 2016, **9**, (5), pp. 1009–1018

[10] Mohamed Basri, H., Mekhilef, S.: 'Experimental evaluation of model predictive current control for a modified three-level four-leg indirect matrix converter', *IET Electr. Power Appl.*, 2018, **12**, (1), pp. 114–123

[11] Liu, Y., Liang, W., Ge, B., *et al.*: 'Quasi-Z-source three-to-single-phase matrix converter and ripple power compensation based on model predictive control', *IEEE Trans. Ind. Electron.*, 2018, **65**, (6), pp. 5146–5156

[12] Su, J., Gao, R., Husain, I.: 'Model predictive control based field-weakening strategy for traction EV used induction motor', *IEEE Trans. Ind. Appl.*, 2018, **54**, (3), pp. 2295–2305

[13] Yan, L., Dou, M., Hua, Z., *et al.*: 'Optimal duty cycle model predictive current control of high-altitude ventilator induction motor with extended minimum stator current operation', *IEEE Trans. Power Electron.*, 2018, **33**, (8), pp. 7240–7251

[14] Mahmoudi, H., Aleenejad, M., Ahmadi, R.: 'Modulated model predictive control for a Z-source-based permanent magnet synchronous motor drive system', *IEEE Trans. Ind. Electron.*, 2018, **65**, (10), pp. 8307–8319

[15] Odhano, S., Bojoi, R., Formentini, A., *et al.*: 'Direct flux and current vector control for induction motor drives using model predictive control theory', *IET Electr. Power Appl.*, 2017, **11**, (8), pp. 1483–1491

[16] Zhang, Z., Fang, H., Gao, F., *et al.*: 'Multiple-vector model predictive power control for grid-tied wind turbine system with enhanced steady-state control performance', *IEEE Trans. Ind. Electron.*, 2017, **64**, (8), pp. 6287–6298

[17] Xu, Y., Wang, J., Zhang, B., *et al.*: 'Three-vector-based model predictive current control for permanent magnet synchronous motor', *Trans. Ch. Electrotech. Soc.*, 2018, **33**, (5), pp. 980–988

[18] Siami, M., Khaburi, D.A., Abbaszadeh, A., *et al.*: 'Robustness improvement of predictive current control using prediction error correction for permanent-magnet synchronous machines', *IEEE Trans. Ind. Electron.*, 2016, **63**, (6), pp. 3458–3466

[19] Chen, Z., Qiu, J., Jin, M.: 'Adaptive finite-control-set model predictive current control for IPMSM drives with inductance variation', *IET Electr. Power Appl.*, 2017, **11**, (5), pp. 874–884

[20] Stati, N., Abdelrahem, M., Mobarak, M.H., *et al.*: 'Finite control set-model predictive control with on-line parameter estimation for variable-speed wind energy conversion systems'. 2016 Int. Symp. on Industrial Electronics (INDEL), Banja Luka, Bosnia and Herzegovina, 2016, pp. 1–6

[21] Wang, J., Wang, F., Zhang, Z., *et al.*: 'Design and implementation of disturbance compensation-based enhanced robust finite control set predictive torque control for induction motor systems', *IEEE Trans. Ind. Inf.*, 2017, **13**, (5), pp. 2645–2656

[22] Cui, R., Chen, L., Yang, C., *et al.*: 'Extended state observer-based integral sliding mode control for an underwater robot with unknown disturbances and uncertain nonlinearities', *IEEE Trans. Ind. Electron.*, 2017, **64**, (8), pp. 6785–6795

[23] Zhang, J., Liu, X., Xia, Y., *et al.*: 'Disturbance observer-based integral sliding-mode control for systems with mismatched disturbances', *IEEE Trans. Ind. Electron.*, 2016, **63**, (11), pp. 7040–7048

[24] Mercorelli, P.: 'A two-stage sliding-mode high-gain observer to reduce uncertainties and disturbances effects for sensorless control in automotive applications', *IEEE Trans. Ind. Electron.*, 2015, **62**, (9), pp. 5929–5940

[25] Wang, J., Li, S., Yang, J., *et al.*: 'Finite-time disturbance observer based non-singular terminal sliding-mode control for pulse width modulation based DC–DC buck converters with mismatched load disturbances', *IET Power Electron.*, 2016, **9**, (9), pp. 1995–2002

[26] da Silva, G.S., Vieira, R.P., Rech, C.: 'Discrete-time sliding-mode observer for capacitor voltage control in modular multilevel converters', *IEEE Trans. Ind. Electron.*, 2018, **65**, (1), pp. 876–886

[27] Yang, H., Zhang, Y., Liang, J., *et al.*: 'Sliding-mode observer based voltage-sensorless model predictive power control of PWM rectifier under unbalanced grid conditions', *IEEE Trans. Ind. Electron.*, 2018, **65**, (7), pp. 5550–5560

[28] Hammouda, W., Ladhari, T., M'sahli, F., *et al.*: 'Second order sliding mode observer based on twisting algorithm for induction motor'. 2015 16th Int. Conf. on Sciences and Techniques of Automatic Control and Computer Engineering (STA), Monastir, Tunisia, 2015, pp. 763–767

[29] Zhao, L., Huang, J., Liu, H., *et al.*: 'Second-order sliding-mode observer with online parameter identification for sensorless induction motor drives', *IEEE Trans. Ind. Electron.*, 2014, **61**, (10), pp. 5280–5289

[30] Zheng, T., Kou, X., Li, Y.: 'Engine cylinder pressure estimation using second-order sliding mode observer based on super-twisting algorithm'. Proceeding of the 11th World Congress on Intelligent Control and Automation, Shenyang, People's Republic of China, 2014, pp. 3886–3891

[31] Yang, R., Wang, M., Li, L., *et al.*: 'Thrust ripple compensation of PMLSM based on second-order sliding mode observer with supertwisting algorithm'. IECON 2017–43rd Annual Conf. of the IEEE Industrial Electronics Society, Beijing, People's Republic of China, 2017, pp. 3698–3703

[32] Levant, A.: 'Robust exact differentiation via sliding mode technique', *Automatica*, 1998, **34**, (3), pp. 379–384

[33] Lascu, C., Blaabjerg, F.: 'Super-twisting sliding mode direct torque control of induction machine drives'. 2014 IEEE Energy Conversion Congress and Exposition (ECCE), Pittsburgh, PA, USA, 2014, pp. 5116–5122

[34] Liang, D., Li, J., Qu, R.: 'Sensorless control of permanent magnet synchronous machine based on second-order sliding-mode observer with online resistance estimation', *IEEE Trans. Ind. Appl.*, 2017, **53**, (4), pp. 3672–3682